CHEMISTRY OF MATERIALS

pubs.acs.org/cm

Article

Synthesis, Electronic Structure, and Redox Chemistry of $Li_2MnP_2S_6$, a Candidate High-Voltage Cathode Material

Yi-Ting Cheng,◆ Yuta Fujii,◆ Yu Nomata,◆ Madhulika Mazumder, Nataly Carolina Rosero-Navarro, Aichi Yamashita, Yoshikazu Mizuguchi, Chikako Moriyoshi, Takato Mitsudome, Toshiaki Ina, Kiyofumi Nitta, Kiyoharu Tadanaga, Akira Miura,* and Christopher J. Bartel*

Cite This: *Chem. Mater.* 2024, 36, 9947−9958

Read Online

ACCESS | Metrics & More | Article Recommendations | Supporting Information

ABSTRACT: While significant efforts have been made to harness the large capacity of sulfide-based cathodes, there has been limited focus on increasing their voltage. Here, by a novel iodide-assisted synthesis route, we successfully synthesized lithium metal thiophosphates $Li_2MP_2S_6$ (M = Mn, Fe, and Co), of which $Li_2MnP_2S_6$ is a new compound. Electrochemical extraction of Li from $Li_2FeP_2S_6$ and $Li_2MnP_2S_6$ was performed at ∼3 V, significantly higher than other sulfide-based cathodes. Despite the similar voltages, these two materials were found to operate by very different redox mechanisms. Density functional theory calculations and X-ray absorption spectroscopy show that while $Li_2FeP_2S_6$ exhibits mostly traditional cationic redox, $Li_2MnP_2S_6$ redox involves significant participation of anionic redox. Our analysis of $Li_2MnP_2S_6$ is also used to contextualize recent work on other Li-rich thiophosphate cathodes. This work introduces a new synthetic route to access sulfide-based materials and sheds insights into the high-voltage redox mechanism in thiophosphate-based cathodes.

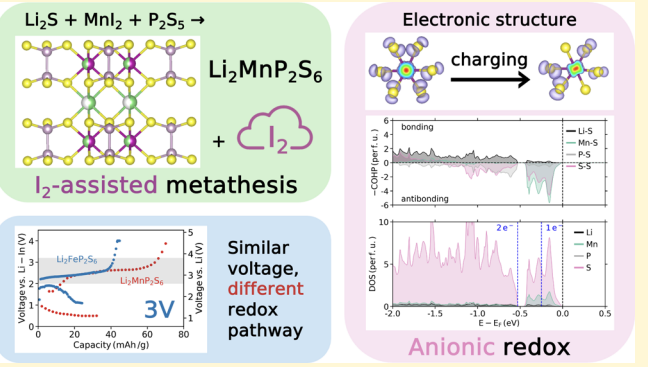

INTRODUCTION

High-voltage cathode materials are essential for the development of energy-dense batteries. Transition metal oxide cathodes, exemplified by $LiCoO_2$ having Co^{3+}/Co^{4+} redox, are typically high-voltage cathodes, operating above 3 V vs Li/Li^+.[1,2] In addition to high voltage, transition metal oxides with "Li excess" (more Li than transition metal per mole) exhibit increased capacity by involving the redox of not only cations at high valence states but also anions.[3−5] In contrast to oxides, sulfide-based cathodes are predominantly low voltage because the metal−sulfur bonds are less ionic than their oxide counterparts (cation redox) and S 3p states occupy significantly higher energy levels compared to O 2p states (anion redox).[6,7] One possible advantage of sulfides over oxides is reversibility of anion redox due to the propensity for S to remain in the solid-state during oxidation (contrasted with irreversible loss of O_2 gas). Reversible S redox has been demonstrated through the formation of electron holes, dimerization of S−S,[7−10] and rehybridization between metal−sulfur states.[11,12]

Fe-based sulfide cathodes are particularly attractive due to their Earth-abundance and their tendency to form stable interfaces with sulfide solid electrolytes like Li_3PS_4 (LPS).[13−16] Although Li_2FeS_2 exhibits relatively high voltage associated with S redox, its voltage is still only around 2.5 V vs Li/Li^+.[10,17] Among various iron sulfides such as FeS,[15] FeS_2,[14,18] $FePS_3$,[16,18] Li_2FeS_2,[17] and $Li_2FeP_2S_6$,[8,19] only $Li_2FeP_2S_6$ shows a high voltage of approximately 3.0 V vs Li/Li^+. In a previous report, the high voltage of $Li_2FeP_2S_6$ is explained by the Fe^{2+}/Fe^{3+} redox couple, assuming that the strong covalent bonding of P−S in the $[P_2S_6]^{4-}$ anion contributes to raising the Fe^{2+}/Fe^{3+} redox potential.[19,20] Other transition metal sulfides beyond Fe have been explored but show voltages < ∼ 2.5 V vs Li/Li^+.[10−12,21,22] For example, the layered structure of $MnPS_3$ demonstrates a highly reversible capacity and rapid insertion/extraction of alkali metal ions, making it a promising anode material, but its low voltage precludes it from application as a cathode.[23,24] This work focuses on synthesizing and characterizing thiophosphate-based cathode materials to aid in the development of high-voltage transition metal sulfide cathodes.

$Li_2MP_2S_6$, where M is a divalent metal, can be considered a solid solution between layered $M_2P_2S_6$ (c.f. $FePS_3$, $NiPS_3$, and

Received: August 22, 2024
Revised: September 9, 2024
Accepted: September 10, 2024
Published: September 18, 2024

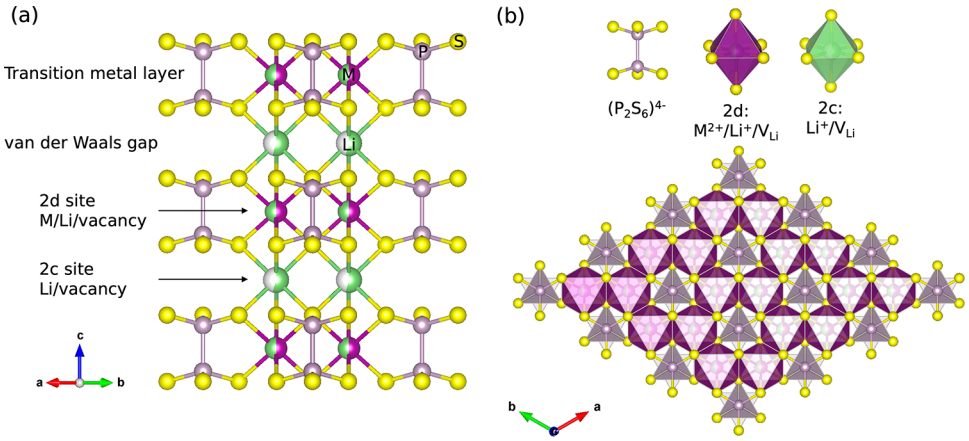

Figure 1. Crystal structure of $Li_2MP_2S_6$ (M = divalent transition metals: Mn, Fe, and Co) (a) along the middle of the *a*-axis and the *b*-axis demonstrating the layered structure and (b) down the *c*-axis showing the honeycomb structure and the trigonal symmetry of $Li_2MP_2S_6$. Note that these phases are known to exhibit off-stoichiometry on the 2*d* site, hence the depiction of partial vacancy occupation on this site. The stoichiometric $Li_2MP_2S_6$ phase would have 0.5 Li and 0.5 *M* occupation on 2*d*.

$Fe_{2-x}Co_xP_2S_6$)[25−29] and $Li_4P_2S_6$ phases (where Li occupies both the *M* and interlayer sites).[30,31] Although $Li_2FeP_2S_6$ was reported around two decades ago,[19] nonstoichiometric compounds like $Li_{1.56}Co_{0.71}P_2S_6$, $Li_{2.26}Fe_{0.94}P_2S_6$ and $Li_2Fe_{0.8}Mn_{0.2}P_2S_6$ were recently reported as isostructural compounds.[8,32] These compounds were synthesized through solid-state reactions using Li_2S, *M*, and P_2S_5 in a stoichiometric ratio at ∼700 °C.[8,19,32]

For $Li_2FeP_2S_6$, Takada et al. showed that 0.7 Li^+ can be extracted at a high voltage of ∼3 V, presumably making use of the inductively stabilized Fe^{2+}/Fe^{3+} redox couple.[19] Zarabadi-Poor et al. recently demonstrated that upon Mn-substitution, $Li_2Fe_{0.8}Mn_{0.2}P_2S_6$ exhibits a much higher capacity (∼1.65 Li^+ extraction in the first cycle) than $Li_2FeP_2S_6$, while maintaining the ∼3 V plateau.[8] However, the redox mechanism appears quite complicated. Although different octahedral crystal field splitting of Fe and Mn is expected, it is difficult to rationalize the role of Mn in facilitating expanded high-voltage capacity.

In this work, we synthesized three lithium-containing transition-metal thiophosphates, $Li_2MP_2S_6$ (M = Mn, Fe, Co), using a novel I_2-assisted synthesis and discovered $Li_2MnP_2S_6$ as a new compound. We examined the electrochemical behavior of the Fe and Mn thiophosphates during Li^+ extraction using electrochemical cycling in an all-solid-state cell, *ex situ* characterization, and electronic structure calculations. Surprisingly, although Li was extracted from $Li_2FeP_2S_6$ and $Li_2MnP_2S_6$ at similar voltages, the redox mechanism appears significantly different between the two materials. While $Li_2FeP_2S_6$ mainly exhibits traditional transition metal redox behavior, $Li_2MnP_2S_6$ follows a mixed cationic and anionic redox route.

RESULTS

Structure and Synthesis of $Li_2MP_2S_6$. $Li_2MP_2S_6$ adopts a CdI_2-like structure, and features a layered-honeycomb and trigonal arrangement ($P\bar{3}1m$).[8,19,32] In Figure 1a, we illustrate the alternating transition metal layers and van der Waals gaps in the structure along the *c* direction. Li, *M*, and vacancies can occupy the same sites, leading to significant structural complexity. Li can occupy the Wyckoff position 2*d* within the transition metal layer or Wyckoff position 2*c* in the van der Waals gap. While the 2*c* sites are half-occupied by Li and vacancies in the $Li_2MP_2S_6$ structure, the 2*d* sites consist of partially occupied Li/*M* sites, separated by P−P dumbbells. Both Li and *M* are octahedrally coordinated by S, as illustrated in Figure 1b.

Previous work on $Li_2MP_2S_6$ has focused on a "traditional" solid-state synthesis route, starting from Li_2S, *M*, and P_2S_5. To expand the library of known lithium thiophosphates, we explored alternative synthetic approaches based on the concept of metathesis. Metathesis increases the thermodynamic driving force for materials synthesis by yielding highly stable byproducts that can be washed away (e.g., LiCl) and has the potential advantage of avoiding stable impurities by shifting the thermodynamic landscape for synthesis.[33,34] In this work, $Li_2MP_2S_6$ (M = Mn, Fe, Co) synthesis was first attempted by heating a mixture of Li_2S, MCl_2, and P_2S_5 at 460 °C with a molar ratio of 2:1:1 in an evacuated quartz tube and can be expressed by the following reaction:

$$2Li_2S + MCl_2 + P_2S_5 \rightarrow Li_2MP_2S_6 + 2LiCl + S, \text{ where } M = Mn, Fe, Co$$

X-ray diffraction (XRD) patterns of the product $Li_xM_yP_2S_6$ (M = (i) Mn, (ii) Fe, (iii) Co) phases are depicted in Figure S1. The diffraction patterns of the obtained powders for $Li_xMn_yP_2S_6$ and $Li_xFe_yP_2S_6$ contained two phases, which are identified as hexagonal and rock-salt phases. The hexagonal phase corresponds to the structure of $Li_xM_yP_2S_6$, while the rock-salt phase was attributed to LiCl as the byproduct. For comparison, XRD patterns of $Li_2FeP_2S_6$ (ICSD #98450) with a hexagonal phase and LiCl (ICSD #26909) with a rock salt phase are also shown in Figure S1. In the diffraction patterns for $Li_xCo_yP_2S_6$, unknown peaks were observed that do not correspond to the two phases (hexagonal and rock-salt phases). Although S is a byproduct of the reaction as written, it cannot be detected in the XRD patterns. During the heating process at 460 °C, part of the evacuated quartz tubes containing the starting materials was set outside the tubular furnace. As a result, after the heating process, S was precipitated at the end of the quartz tubes outside the tubular furnace due to its low boiling point (445 °C at atmospheric pressure).

https://doi.org/10.1021/acs.chemmater.4c02366
Chem. Mater. 2024, 36, 9947−9958

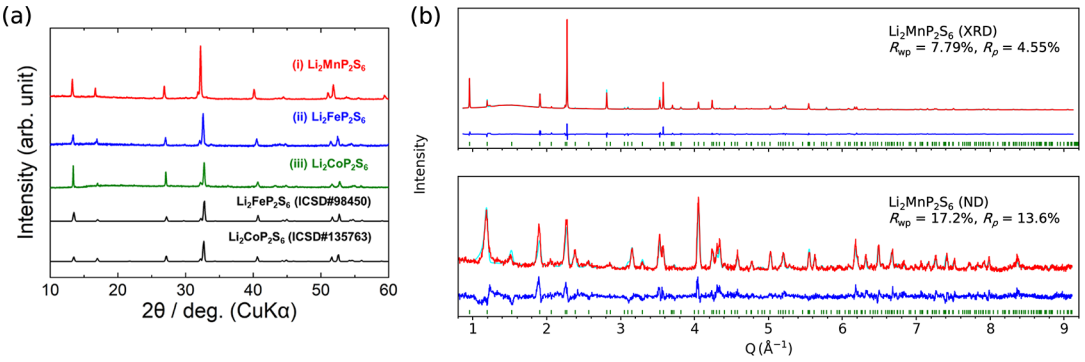

Figure 2. (a) XRD patterns of $Li_2MP_2S_6$ (M = (i) Mn, (ii) Fe, and (iii) Co) powders synthesized from the mixture of Li_2S, MI_2 and P_2S_5 with a molar ratio of 1:1:1. $Li_2MP_2S_6$ (M = Fe (ICSD #98450) and Co (ICSD #135763)) are shown as the reference state. (b) Rietveld refinement profile of $Li_2MnP_2S_6$ by synchrotron XRD with the wavelength of 0.0354244 nm and neutron diffraction (ND) with 0.134177 nm. Observed (red), calculated (sky-blue), and the difference between observed and calculated (blue) patterns. Green vertical bars denote the positions of Bragg reflections. We have uploaded the structure of $Li_2MnP_2S_6$ to the Cambridge Structural Database (CCDC) under deposition number 2378225.

These experiments show that while we failed to synthesize $Li_2CoP_2S_6$, $Li_2FeP_2S_6$ (previously reported) and $Li_2MnP_2S_6$ (newly reported) can be made using solid-state metathesis, however their formation is concomitant with a solid LiCl byproduct that requires removal. Note that during the review of this manuscript, $Li_2MnP_2S_6$ was synthesized in an apparently distinct structure ($R\bar{3}$) along with LiCl byproduct also using solid-state metathesis.[35] To avoid the formation of stable solid byproducts, we replaced MCl_2 with MI_2 and modified the molar ratios to 1:1:1 to target the following reaction equation:

$$Li_2S + MI_2 + P_2S_5 \rightarrow Li_2MP_2S_6 + I_2, \text{ where } M = Mn, Fe, Co$$

In Figure 2a, we show the XRD patterns of the as-prepared $Li_2MP_2S_6$ powders. The XRD patterns of $Li_2MP_2S_6$ (M = Fe (ICSD #98450) and Co (ICSD #135763)) from the ICSD database are shown as reference states for comparison. The diffraction patterns of the obtained powders were identified as a hexagonal phase, indicating the presence of $Li_2MP_2S_6$. Among the transition metals, $Li_2MnP_2S_6$ is a newly discovered compound, whereas $Li_2FeP_2S_6$[8,19,32] and $Li_2CoP_2S_6$[32] have been reported previously. Note that the peaks corresponding to LiI and $I_{(s)}$ were not observed, consistent with the inherent removal of the metathesis byproduct, I_2, in the gas phase. As indicated in Figure 2a, *M*= Mn, Fe, and Co leads to mostly phase-pure $Li_2MP_2S_6$. Upon heating of the quartz tube with a temperature gradient, the main product, $Li_2MP_2S_6$, was formed in the high-temperature region (460 °C) while a small amount of $I_{(s)}$ was precipitated in the low-temperature region (~25 °C) as depicted in Figure S2. To our knowledge this is the first report of I_2-assisted metathesis, which maintains the favorable properties of conventional solid-state metathesis with the added advantage of having only gaseous byproducts. We also attempted the traditional solid-state synthesis method for $Li_2MnP_2S_6$ from Li_2S, MnS, and P_2S_5 in a stoichiometric 1:1:1 ratio, but the synthesis yielded a mixture of $Li_2MnP_2S_6$ with noticeable amounts of unknown phase(s) (Figure S3).

Density functional theory (DFT) calculations were performed to compute the thermodynamic stability of these $Li_2MP_2S_6$ materials and understand the effect of synthetic approach on thermodynamic driving forces to form the target phases. Li−*M*−P−S (M = Mn, Fe, Co) phase diagrams computed with the r^{2}SCAN meta-generalized gradient approximation (meta-GGA) functional[36] reveal that $Li_2MnP_2S_6$ and $Li_2FeP_2S_6$ are thermodynamically stable (decomposition energies[37] of −31 meV/atom and −30 meV/atom, respectively) while $Li_2CoP_2S_6$ is weakly metastable (decomposition energy of +11 meV/atom). Li_3PS_4 appears as a significant competing phase for all targets but was not observed after any of our synthesis experiments.

In Figure S4, we compare the thermodynamic driving forces for "traditional" solid-state synthesis (starting from Li_2S + *MS* + P_2S_5), metathesis with a LiCl byproduct (starting from Li_2S + MCl_2 + P_2S_5), and metathesis with an $I_{2(g)}$ byproduct (starting from Li_2S + MI_2 + P_2S_5). At low temperature, the traditional and iodide routes have comparable driving force (≈ − 0.5 eV/$Li_2MP_2S_6$), with the chloride route being by far the most favorable (≈ − 2 eV/$Li_2MP_2S_6$) due to the formation of LiCl as a byproduct. As temperature is increased, the I_2-assisated route becomes more favorable as the entropy of gaseous I_2 lowers the I_2 free energy by ≈1.4 eV/mol between room temperature and 500 °C.[38] This entropic benefit increases the reactivity of the MI_2 precursor to drive the reaction toward the desired target and results in significantly more thermodynamic driving force for the I_2-assisted route compared to traditional synthesis above ~500 °C.

In Figure S5, we show the scanning electron microscope (SEM) images of the as-synthesized $Li_2MP_2S_6$ (M = (a) Mn, (b) Fe, and (c) Co). The particle sizes of the $Li_2MnP_2S_6$ and $Li_2CoP_2S_6$ powders were primarily in the range of 2−3 μm, while the particle sizes of $Li_2FeP_2S_6$ powders were mainly 5−10 μm. The plate-like shape of some crystals may be indicative of crystallization from a flux, which could result from the low melting point of P_2S_5 (~288 °C). Table S1 presents a summary of the semiquantitative elemental analysis of $Li_xM_yP_2S_6$ from energy dispersive X-ray analysis (EDX) (*M*:P:S) and inductively coupled plasma (ICP) (Li:*M*) analysis. The values of *x* and *y* are close to two and one, respectively (indicative of the expected 2:1 Li:*M* ratio).

To further characterize the structure of $Li_2MnP_2S_6$, we performed Rietveld refinement of synchrotron XRD and neutron diffraction (ND) using the isostructural crystal model of the previously reported $Li_2FeP_2S_6$ with the space group of $P\bar{3}1m$, as shown in Figure 2. The lattice parameters were *a* = 6.08801(9) and *c* = 6.58896(16) Å. The proposed layered compound is composed of $[P_2S_6]^{4-}$, the intralayer 2*d*

https://doi.org/10.1021/acs.chemmater.4c02366
Chem. Mater. 2024, 36, 9947−9958

site of Li/Mn, and the van der Waals layer site (2*c*), as described in Figure 1. The Wyckoff positions, displacement factors, and occupancies of each site from XRD analysis are listed in Table S2, and the bond lengths between P−P, P−S, and *M*−S of the as-synthesized $Li_2MP_2S_6$ are summarized in Table S3.

Given the presence of two distinct sites for Li ions, we used DFT to compute the energies of various Li/*M*/vacancy orderings as a function of Li concentration ($0 < x \leq 2$ in $Li_xMP_2S_6$, M = Mn and Fe). Our calculations reveal that the ground-state structure for all Li concentrations (x) minimizes the occupation of Li in the 2*c* site (see Figure S6 for the energy differences). The result suggests that it is thermodynamically preferred to extract Li from the van der Waals layer (2*c*). The 2*c* site can accommodate up to 1 Li per $Li_xMP_2S_6$, so the material is predicted to become layered for $x < 1$ (i.e., the 2*c* site is unoccupied). These computed energetics are also in agreement with experimental findings for the previously reported $Li_2FeP_2S_6$ and newly refined $Li_2MnP_2S_6$, where the two 2*d* sites were found to be fully occupied (1 Li + 1 *M*) and the two 2*c* sites half-occupied (1 Li + 1 V_{Li}).[8]

Electrochemistry and Cathode Performance of $Li_2MP_2S_6$. The galvanostatic intermittent titration technique (GITT) was applied to measure the quasi-equilibrium voltage without the effect of overpotential (see traces in Figure S7 and a schematic of the cell configuration in Figure S8). In Figure 3a, we show the quasi-equilibrium voltage for $Li_2MP_2S_6$ (M = Mn and Fe) during the first charging and discharging cycle. Similar experiments were performed with M = Co and Ni as well (Figure S9), but given the relatively low capacity (<20 mAh/g), our primary focus will be on studying the electrochemistry and redox mechanisms for *M* = Mn and Fe. For both $Li_2MnP_2S_6$ and $Li_2FeP_2S_6$, the charging plateau occurs at approximately 3.0 V vs Li/Li^+ with a capacity of 70 and 40 mAh/g, respectively. For both compounds, the discharge capacities were found to be ∼30 mAh/g, much smaller than the first-cycle charge capacities. During subsequent discharge, both the capacity and potential were low, indicative of significant irreversibility. Importantly, the redox potential of the solid electrolyte, amorphous LPS, is approximately 2 V,[39] indicating that the electrolyte is not the origin of the observed capacity. To complement the experimental measurements, voltage profiles for M = Mn and Fe computed using DFT with the r^{2}SCAN+U functional are shown in Figure 3b (with the corresponding convex hulls shown in Figure S10). Despite the change in transition metal, the calculated voltages remain around 3 V (∼300 mV larger for M = Mn), which is consistent with the experimentally observed voltages (Figure 3a) and similar recent studies on $Li_2FeP_2S_6$.[8]

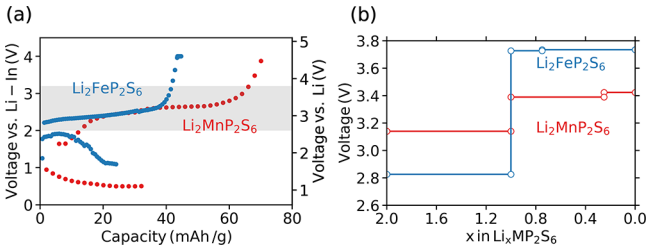

Figure 3. (a) Quasi-equilibrium voltage of $Li_2MP_2S_6$ (*M* = Mn and Fe) during electrochemical Li extraction and subsequent insertion was measured at a current density of 12.7 μA cm^{-2} and estimated C rate of ∼0.024 C at 60 °C. The scale of capacity is shown at the bottom of the figure. The voltage interval 2.6 to 3.8 V is colored in gray for comparison to the calculated voltage. The maximum observed capacities for M = Mn and Fe with 70 and 40 mAh/g respectively, correspond to the removal of approximately 0.85 and 0.5 Li^+ per $Li_2MP_2S_6$ unit formula. (b) DFT-calculated voltage curve of $Li_2MP_2S_6$ (*M* = Mn and Fe) with the r^{2}SCAN+U functional.

The cycle performance of the cell utilizing $Li_2MnP_2S_6$, which exhibits the highest capacities among $Li_2MP_2S_6$, was further investigated under a smaller current density of 6.4 μA/cm^2 at 60 °C. As shown in Figure 4, there is clearly a fade in capacity with increasing cycle number. The shift in the voltage profile and the position of the voltage plateau suggest irreversible reactions that may be associated with a transition from octahedral to trigonal MS_6 similar to that exhibited by $FePS_3$ upon Li insertion.[27] During the second and subsequent cycles, the drop in voltage may be associated with the decomposition of $Li_2MnP_2S_6$ into Li_2S and $MnPS_3$, which operates at a lower voltage.[23,24] These are initial indications, but more work is needed to understand the cyclability of $Li_2MnP_2S_6$.

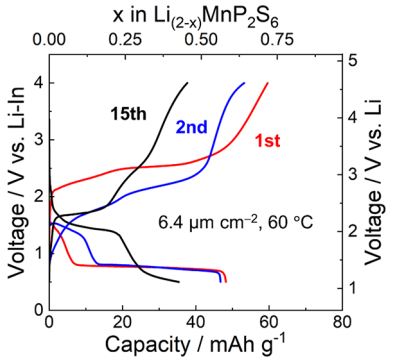

Figure 4. Discharge−charge profile for the all-solid-state cell using $Li_2MnP_2S_6$ during the first, second, and the 15th cycle under the current density of 6.4 μA cm^{-2} and estimated C rate of ∼0.012 C at 60 °C.

Electronic Structure and Redox Mechanism of $Li_2MP_2S_6$. To investigate the redox mechanism of $Li_2MnP_2S_6$, we performed XRD and X-ray absorption near edge structure (XANES) measurements at three points along the first-cycle voltage curves, as shown in Figure 5. In Figure 5b, we show XRD patterns of $Li_2MnP_2S_6$ before and after one charge−discharge cycle to assess structural changes during Li cycling. After the first charge, the 001 peak (∼3.085°) shifts slightly to a higher angle, consistent with contraction along the *c* direction (see Table S4) and indicative of Li extraction from the 2*c* site (consistent with our calculated Li site energies). Subsequent discharge does not significantly alter the diffraction pattern, indicating that the Li^+ ions are only partially inserted back into the van der Waals layer, consistent with the smaller discharge than charge capacity. In Figure 5c and 5d, we show the Mn K-edge and S K-edge XANES spectra of the $Li_xMn_2P_2S_6$ composite electrodes measured before and after the first charge cycle. In the Mn K-edge, the absorption spectra (i) before and (ii) after the first charge do not indicate Mn redox activity. When comparing to the absorption edges of MnS and Mn_2O_3 (representing Mn^{2+} and Mn^{3+}, respectively), these edges are similar to the spectrum of MnS, suggesting Mn remains 2+ throughout the first charge cycle. In contrast, published work on $Li_2FeP_2S_6$ shows that charging induces a change in the Fe K-edge XANES indicative of $Fe^{2+/3+}$ redox.[8]

https://doi.org/10.1021/acs.chemmater.4c02366
Chem. Mater. 2024, 36, 9947−9958

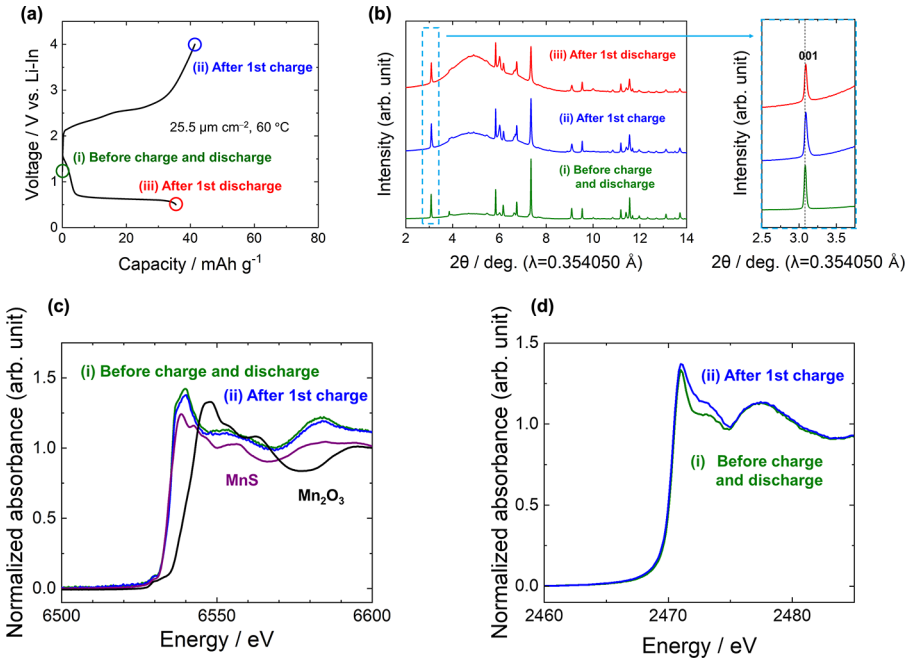

Figure 5. (a) The discharge−charge profile for the all-solid-state cell using $Li_2MnP_2S_6$ during the first cycle under the current density of 25.5 μA cm^{-2} at 60 °C. The circles in (a) shows the XRD measurement points. (b) XRD patterns of the $Li_xMnP_2S_6$ composite electrodes before and after the first charge and discharge process. Inset is the expansion of the 001 peaks. (c) Mn K-edge and (d) S K-edge XANES spectra of the $Li_xMnP_2S_6$ composite electrodes before and after the first charge cycle. The K-edge positions of MnS and Mn_2O_3 are displayed as indicators of Mn^{2+} and Mn^{3+}, respectively.

The lack of redox activity for Mn suggests that the Li capacity observed for $Li_2MnP_2S_6$ is associated with (poly)anion redox. The S K-edge spectrum shows an increase absorbance at the 2472 eV bump after the first charge, supporting that S^{2-} is oxidized, and anion states contribute significantly to the redox process.

To understand the difference between the redox mechanisms of M = Fe and Mn, we compared the electronic structures of these materials as a function of Li concentration. In Figure 6, we computed the electronic structure of the fully discharged $Li_2FeP_2S_6$ (a) and $Li_2MnP_2S_6$ (b) with the HSE06 functional[40] and partial charge densities, density of states (DOS), and Crystal Orbital Hamilton Population (COHP) analysis.[41−43] Within the rigid band approximation, Li^+ extraction should be compensated by the oxidation of the highest energy occupied e^- in the fully discharged cathode materials. To examine these electronic states, we integrate the DOS down in energy from the Fermi level (taken to be the valence band maximum), and lines are drawn in Figure 6a and 6b to indicate the electronic states expected to compensate for the extraction of 1 Li^+ (1 e^-) and 2 Li^+ (2 e^-).

As shown in Figure 6a, the DOS for M = Fe indicates that Fe d states are prevalent near the Fermi level (∼1 e^-), consistent with charge compensation for the extraction of the first Li arising from Fe^{2+}/Fe^{3+} redox.[8] The COHP (Figure 6a) and partial charge analysis (Figure 6c) of this first e^- shows that nonbonding (not aligning with ligands) Fe states coexist with weak S−S and Fe−S antibonding states. This is consistent with crystal field theory suggesting the highest energy occupied e^- in Fe^{2+} is in a nonbonding t_{2g} state.[44] Based on the experimental voltage curve (Figure 3a), we know that only 0.5 Li (∼40 mAh/g) could be extracted when M = Fe. While 1 e^- of Fe-rich states were calculated to be present near the Fermi level of $Li_2FeP_2S_6$, elemental analysis of the M = Fe thiophosphate suggests it may be Fe-deficient, perhaps explaining the failure to achieve the removal of 1 Li experimentally via Fe^{2+}/Fe^{3+} redox.

After extracting 1 Li^+ ($LiFeP_2S_6$, see the right part of Figure 6c), the Fe orbital shape changes into that of e_g states, indicating that the t_{2g} e^- underwent oxidation. Probing the charge density of the half-charged structure (1st e^- of $LiFeP_2S_6$) suggests that the first Li^+ extraction induces rehybridization that further populates S−S states. The S electronic states begin to dominate and the orientation of these orbitals indicates a mixture of antibonding Fe−S, antibonding S−S, and nonbonding S states. In Figure S11, we also show the DOS and COHP of these same states in the half-charged $LiFeP_2S_6$. Upon one Li removal from $Li_2FeP_2S_6$ to form $LiFeP_2S_6$, the predominant Fe states (nonbonding Fe and antibonding Fe−S and S−S states) in the conduction band again suggest that Fe undergoes oxidation. Together, this analysis suggests that significant anion redox would be required to extract the second Li^+ from $Li_2FeP_2S_6$, and these states do not appear to be redox-active based on the electrochemical experiments performed here and previously.[8,19]

In contrast, $Li_2MnP_2S_6$ shows a more complicated picture. In Figure 6b, we present an analogous look at the electronic structure of $Li_2MnP_2S_6$. As the transition metal is changed from Fe to Mn, there is a downward shift in the energy level of the occupied M d states relative to that of the occupied S p states (Mn^{2+} lacks the high-energy t_{2g} e^- seen for Fe^{2+}). As a result, the states near the Fermi level are dominated by S-rich states. While for M = Fe, the DOS corresponding with 1 e^- oxidation is consistent with traditional transition metal (Fe) redox, for M = Mn, both the first and second e^- near the Fermi level exhibit substantially more S than M character. From the COHP analysis shown in Figure 6b, the mixed Mn and S states just below the Fermi level in the DOS correspond to

https://doi.org/10.1021/acs.chemmater.4c02366
Chem. Mater. 2024, 36, 9947−9958

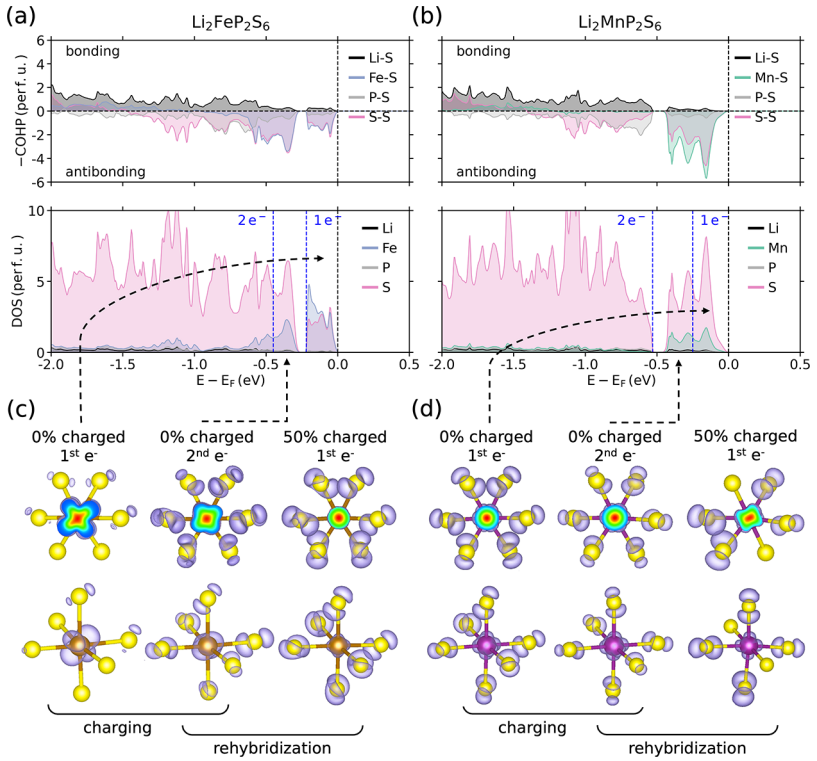

Figure 6. Element-projected DOS and COHP for fully discharged Li metal thiophosphate (a) $Li_2FeP_2S_6$ and (b) $Li_2MnP_2S_6$. The DOS is normalized per $Li_2MP_2S_6$ formula unit, and the energy is presented relative to the Fermi energy (E_F) of each compound. The element-projected DOS (and COHP) for Li, Fe, Mn, P, and S, (and their bonding with S) are colored in black, blue, green, gray, and pink, respectively. The blue dashed lines show the energy corresponding to 1 e^- and 2 e^- below E_F and point out the energy depth that is required to extract one and two Li ions from the cathode materials. The conduction band states begin at 2.9 and 3.3 eV above the Fermi energy for $Li_2FeP_2S_6$ and $Li_2MnP_2S_6$, respectively, but are excluded for clarity. The states with −COHP > 0 denotes bonding states and those with −COHP < 0 are the antibonding states. Evolution of partial charge density between (c) $Li_2FeP_2S_6$ and $LiFeP_2S_6$, and (d) $Li_2MnP_2S_6$ and $LiMnP_2S_6$ within the energy window compensating for the extraction of the 1st or 2nd e^- (highest energy occupied states summing to 1st or 2nd e^-) upon removal of 1st or 2nd Li^+. For the cross section, the red color corresponds to more and blue corresponds to less charge density. The isosurface was set as 0.004. The electronic structures are calculated with HSE06.

predominantly Mn−S antibonding states with some additional population of S−S antibonding. These near-Fermi level (1st e^-) states in $Li_2MnP_2S_6$ appear very similar to the second e^- states in $Li_2FeP_2S_6$ (especially after allowing for rehybridization−i.e., the first e^- of half-charged $LiFeP_2S_6$ shown by partial charge analysis in Figure 6c). The experimental voltage curve (Figure 3a) shows that ∼0.85 Li (70 mAh/g) could be extracted from $Li_2MnP_2S_6$ in the first cycle and ∼0.6 Li (50 mAh/g) is removed during the second cycle (Figure 4). According to the electronic structure analysis, these oxidized electrons must originate from S-rich electronic states, including S−S antibonding states. Note that while the $Li_2MP_2S_6$ crystal structure does not contain S−S dimers, the antibonding S−S states observed in COHP can be attributed to the interaction between S orbitals neighboring one another in the MS_6 octahedra, similar to that observed in metal oxide materials.[3,45]

The partial charge density for $Li_{2-x}MnP_2S_6$ shown in Figure 6d depicts the nature of Mn−S and S−S states. In the highest energy states of $Li_2MnP_2S_6$ (Figure 6d, left) summing to 1 e^-, the Mn center is uniformly surrounded with charge density and these Mn orbitals appear strongly hybridized with S (resembling the Fe^{3+} e_g states in half-charged $LiFeP_2S_6$). From the DOS and COHP, we can deduce that this 1 e^- involves a mixture of Mn−S and S−S antibonding states. We also observe that the coupling of S lone pairs between adjacent ligands in the octahedron provide the S−S states. As with $Li_2FeP_2S_6$, comparison of the second e^- in the fully discharged phase (Figure 6d, middle) and the first e^- in the half-charged phase (Figure 6d, right) reveals rehybridization upon Li^+ removal. For $Li_2MnP_2S_6$, this rehybridization localizes the Mn e^- to certain S ligands. The DOS and COHP of these electronic states in half-charged $LiMnP_2S_6$ are shown in Figure S12 to support their proposed bonding character.

These results suggest that both Mn and S participate in the charge compensation mechanism, and the octahedral complex undergoes significant rehybridization upon Li^+ extraction. This rehybridization may occur as a result of the instability of Mn^{3+} in sulfides (to our knowledge, $K_{2x}Mn_xSn_{3-x}S_6$ is the only known example in a compound that does not also contain a more electronegative anion such as oxygen).[46] A resistance to forming Mn^{3+} is supported by the *ex situ* XANES measurements (Figure 5c) as well as the computed Bader charge for Mn in $Li_xMnP_2S_6$ (see Figure S13a computed with the r^{2}SCAN+U functional). The fact that there is no change in the oxidation states of Mn^{2+} despite the involvement of Mn−S states may be attributed to the "self-regulating response".[47] As Li^+ ions are extracted, there is a corresponding removal of electron charge from $Li_2MnP_2S_6$. This process induces rehybridization of the Mn−S states, effectively maintaining the oxidation state of Mn^{2+}. Inspection of computed magnetic moments does show a decrease in magnetization for Mn in $LiMnP_2S_6$ compared to $Li_2MnP_2S_6$ (see Figure S13b), which is

https://doi.org/10.1021/acs.chemmater.4c02366
Chem. Mater. 2024, 36, 9947−9958

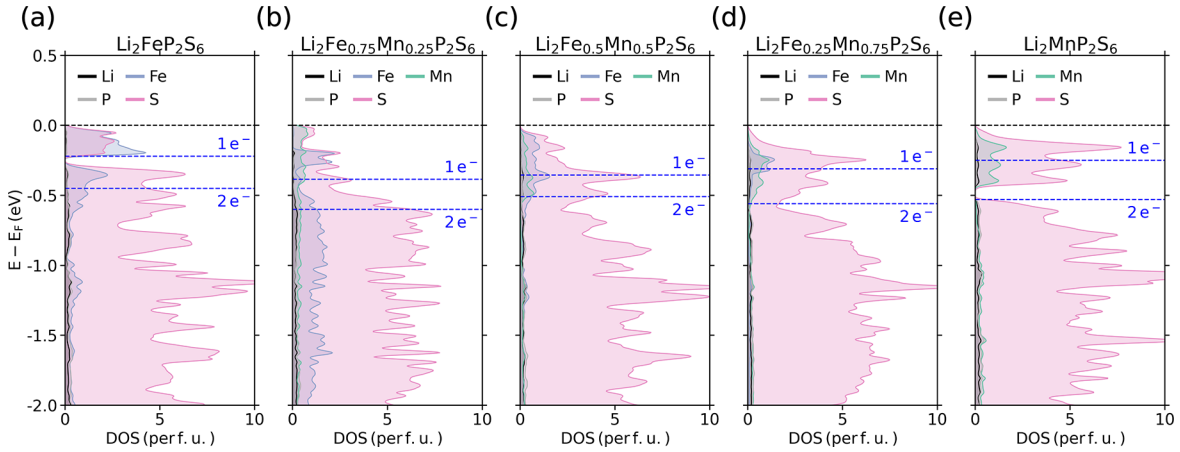

Figure 7. Element-projected DOS of fully discharged $Li_2Fe_{1-y}Mn_yP_2S_6$: (a) $Li_2FeP_2S_6$, (b) $Li_2Fe_{0.75}Mn_{0.25}P_2S_6$, (c) $Li_2Fe_{0.5}Mn_{0.5}P_2S_6$, (d) $Li_2Fe_{0.25}Mn_{0.75}P_2S_6$, and (e) $Li_2MnP_2S_6$ calculated with HSE06. The DOS is normalized per $Li_2Fe_{1-y}Mn_yP_2S_6$ formula unit, and the energy is presented relative to the Fermi energy (E_F) of each compound. The element-projected DOS for Li, Fe, Mn, P, and S are colored in black, blue, green, gray, and pink, respectively. The blue dashed lines show the energy corresponding to 1 e^- and 2 e^- below E_F and point out the energy depth that is required to extract one and two Li ions from the cathode materials. The conduction band states begin at 2.8, 2.8, and 2.7 eV above the Fermi energy for $Li_2Fe_{0.75}Mn_{0.25}P_2S_6$, $Li_2Fe_{0.5}Mn_{0.5}P_2S_6$, and $Li_2Fe_{0.25}Mn_{0.75}P_2S_6$, respectively, but are excluded for clarity.

likely a consequence of the rehybridization (change in the ligand field) rather than oxidation to Mn^{3+}. Along with the observation of a shift in the S K-edge XANES, these results suggest that anion redox contributes to the observed capacity from the outset of charging $Li_2MnP_2S_6$. Investigation of the deeper electronic states suggests that continued Li extraction would continue to require anion redox.

In short, the charge compensation mechanism for M = Fe is found to transition from mainly cationic redox for the first Li extraction to mixed cationic/anionic redox for the second. For M = Mn, our findings suggest a relatively fixed redox mechanism involving mixed cation/anion redox for the extraction of both the first and second Li. This is further supported by the smaller increase in voltage after extracting 1 Li for $Li_2MnP_2S_6$ compared with $Li_2FeP_2S_6$ (see Figure 3b).

Very recent work showed that partial substitution of Fe by Mn in $Li_2FeP_2S_6$ (i.e., $Li_2Fe_{0.8}Mn_{0.2}P_2S_6$) increases the charge capacity significantly, beyond what would be expected from purely Fe redox (~0.8 Li) or combined Fe and Mn cationic redox (0.8 + 0.2 Li).[8] To understand the potentially cooperative effect of Fe/Mn mixing on electrochemical capacity, we performed a similar thermodynamic and electronic structure analysis of $Li_2Fe_{1-y}Mn_yP_2S_6$ materials (y = 0.25, 0.5, and 0.75). In Figure 7, we show the DOS of fully discharged $Li_2Fe_{1-y}Mn_yP_2S_6$ ranging from y = 0 (purely Fe) to y = 1 (purely Mn). In the Mn-dominated mixed phases (y = 0.50, 0.75, Figure 7**c-d**), the near-Fermi level states are dominated by S (as with $Li_2MnP_2S_6$). Investigating the COHP (Figure S14) supports that these states arise from Mn−S and S−S antibonding interactions. At a similar energy level are Fe states, which from COHP analysis appear as mostly nonbonding (as with $Li_2FeP_2S_6$). In $Li_2Fe_{0.75}Mn_{0.25}P_2S_6$ (the composition most similar to the high capacity material studied in ref.,[8] the Mn-substitution induces rehybridization of Fe−S states such that predominantly Mn and S states lie at the Fermi level (Figure 7b). Interestingly, when inspecting the conduction band (oxidized) states of half-charged $LiFe_{0.75}Mn_{0.25}P_2S_6$, Fe states dominate, suggesting that these are still the first to be oxidized upon Li^+ removal (Figure S15). As such, the first ~0.75 Li capacity in this material can likely be attributed to mainly traditional Fe^{2+}/Fe^{3+} redox (as in $Li_2FeP_2S_6$). In ref.,[8] the additional capacity was attributed to a collective oxidation of the $[P_2S_6]^{4-}$ ligand through interlayer S−S bridging. Our results for $Li_2MnP_2S_6$ indicate that it may be possible for charge compensation to occur without the formation of interlayer S−S dimers. Our experimental results suggest that at least 0.85 Li can be extracted from $Li_2MnP_2S_6$, and our corresponding electronic structure analysis indicates a rehybridization redox mechanism facilitated by S−S and Mn−S interactions within a given MnS_6 octahedron. Inspection of the DOS for the $Li_2Fe_{1-y}Mn_yP_2S_6$ phases shows that additional antibonding Fe states (that are not redox active in $Li_2FeP_2S_6$) lie just below these S−S and Mn−S states, and as a result, may couple with similar M−S and S−S states in the neighboring FeS_6 octahedra in $Li_2Fe_{0.75}Mn_{0.25}P_2S_6$.[11]

DISCUSSION

I_2-Assisted Metathesis. A common strategy for synthesizing metastable or weakly stable phases involves so-called "hyperdimensional" reactions[33] that result in the formation of stable byproducts, such as NaCl.[34] Solid-state metathesis is a typical example in which the valence of cations and anions typically remain unchanged. Other exchange reactions do involve oxidation−reduction processes, such as the formation of nitrides from $NaNH_2$.[48] These exchange reactions can be effective by increasing the thermodynamic driving force (free energy or enthalpy) for the reaction to proceed,[34,49] shifting the thermodynamic landscape to avoid stable competing phases (plausible impurities),[34] or bridging chemical potentials between precursors and the target phase.[50] A limitation of this approach is the need to remove the byproduct(s), typically by washing with water. While in some cases (e.g., most oxides) this adds minimal complication, materials that can react with water (e.g., many nonoxides including $Li_2MP_2S_6$) generally cannot be made phase-pure through typical metathesis reactions, especially if surface chemistry is important for a given application. In this work, we show how the evolution of I_2 at moderate temperatures can be used to similarly drive the reaction but with only volatile byproducts. Metathesis reactions with volatile byproducts (I_2 vapor as demonstrated

https://doi.org/10.1021/acs.chemmater.4c02366
Chem. Mater. 2024, 36, 9947−9958

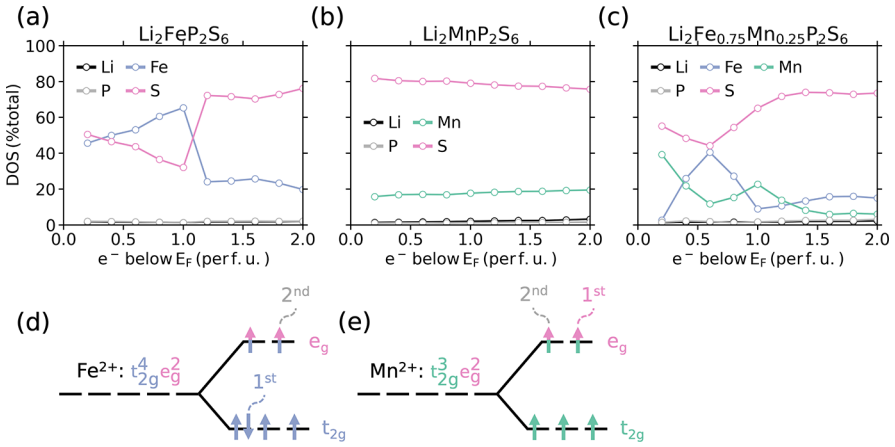

Figure 8. Integrated DOS for fully discharged Li metal thiophosphates (a) $Li_2FeP_2S_6$, (b) $Li_2MnP_2S_6$, and (c) $Li_2Fe_{0.75}Mn_{0.25}P_2S_6$ calculated with HSE06. The percentage of each element in the integrated DOS shows the tendency for oxidation of each ion during charging (moving left to right). Crystal field splitting of the metal *d* orbitals in an octahedral configuration: (d) Fe^{2+} and (e) Mn^{2+}. "1st" and "2nd" refer to the e^- that compensate the removal of 1 and 2 Li ions per formula unit.

here and $ZnCl_2$ vapor as previously shown[51]) present a route to synthesize water-sensitive products with pristine surfaces, eliminating the need for washing. A series of $Li_2MP_2S_6$ phases were successfully synthesized via I_2-assisted metathesis in this work, and a computational thermodynamic analysis[52] assisted in understanding the role of I_2 evolution in driving phase formation. While $Li_2FeP_2S_6$,[8,19,32] $Li_2CoP_2S_6$,[32] and $Li_2Fe_{0.8}Mn_{0.2}P_2S_6$[8] have been synthesized and reported previously, $Li_2MnP_2S_6$ had not been reported prior to this study.

Toward High-Voltage Sulfides with Multielectron Capacity. Transition metal sulfides are an attractive class of materials for emerging battery cathodes, but a foremost challenge is increasing the energy density by identifying higher voltage materials.[12,53−55] The equilibrium voltages of reported sulfide cathodes are mostly around ∼2−2.5 V, and encompass a variety of physical and electronic mechanisms associated with cation and anion redox.[10] In this (and concurrently emerging[8]) work, a class of thiophosphates ($Li_2FeP_2S_6$, $Li_2MnP_2S_6$, $Li_2Fe_{0.8}Mn_{0.2}P_2S_6$) have demonstrated reversible Li cycling at an equilibrium potential of ∼3 V. As is well-known in oxides, placing an anion (S) in a covalent polyanion ($[P_2S_6]^{4-}$) should lower the position of the transition metal redox couple (e.g., $Fe^{2+/3+}$) via the inductive effect, thereby increasing the voltage associated with this charge compensation mechanism.[20] While the higher voltage can be understood through this "polyanion" effect, the specific redox mechanisms in these materials requires a more subtle interpretation. It is well-known that the Li insertion voltage trend over the 3*d* transition metals is $Fe^{2+} < Mn^{2+} < Co^{2+} < Ni^{2+}$ due to the octahedral crystal field splitting and pairing energy of the sixth e^- for Fe^{2+}.[56,57] However, here we observe that $Li_2FeP_2S_6$ and $Li_2MnP_2S_6$ exhibit approximately the same 3 V plateau, indicating that traditional cationic redox is likely not responsible for the observed extraction of Li from $Li_2MnP_2S_6$.

In our previous work on Mg thiospinel cathodes, quantitively integrating the DOS in the rigid band approximation effectively captured the tendency for anion vs cation oxidation and was connected to the observed Mg^{2+} capacities (or lack thereof) in $MgTi_2S_4$ and $MgCr_2S_4$.[58] In this work, a similar analysis of the percentage of each element-projected DOS during charging is shown in Figure 8 to quantitatively compare the proportion of metal and anion states near the Fermi level.[58] For *M* = Fe, the capacity of $Li_2FeP_2S_6$ observed in this and previous works can mainly be attributed to Fe redox. Integrating the DOS from the Fermi level, the first e^- is mainly associated with the Fe t_{2g} e^- (see the molecular orbital diagram of Fe^{2+} in Figure 8d), below which there is an internal gap in the DOS before encountering the S-rich Fe−S and S−S states that do not appear as electrochemically active in $Li_2FeP_2S_6$. Unlike *M* = Fe, in Figure 8b, we found that from the outset of Li extraction, charge compensation in $Li_2MnP_2S_6$ involves significant rehybridization of S-rich Mn−S and S−S states that cannot be ascribed to Mn^{2+}/Mn^{3+} redox. While this rehybridization cannot be captured by the rigid band approximation, the integrated DOS in this approximation remains a useful indicator for predicting cationic and anionic redox mechanisms.

Previous work studying Fe/Mn mixing in $Li_2Fe_{0.8}Mn_{0.2}P_2S_6$ showed an improved charge capacity compared to the pure Fe phase $Li_2FeP_2S_6$, corresponding to the extraction of approximately 1.65 Li ions per formula unit during the first cycle.[8] Through *ex situ* Raman and HAXPES measurements and molecular dynamics simulations, the authors suggested the potential of P_2S_6 polyanionic redox, facilitated by S−S dimer formation. In Figure 8c, our calculations suggest that the capacity could alternatively originate from the Mn−S/S−S states active in $Li_2MnP_2S_6$ bridging the gap between traditional cation redox in $Li_2FeP_2S_6$ and hybridized Fe−S/S−S states that could not be accessed in $Li_2FeP_2S_6$. That is, a plausible sequence of redox processes might be: 1) Fe redox (akin to $Li_2FeP_2S_6$), 2) oxidation and rehybridization of Mn−S/S−S states (akin to $Li_2MnP_2S_6$) and 3) oxidation and rehybridization of Fe−S/S−S states, which are accessible only in the Fe/Mn mixed phase. Recent work with $Li_2Ti(S,Se)_3$ and Li_3NbS_4 shows that this kind of rehybridization and "electronic coupling" is important for activating anion or mixed cation/anion redox in sulfides.[11,12]

Importantly, all $Li_2MP_2S_6$ materials studied thus far exhibit some degree of irreversibility indicative of significant structural transformations during electrochemical cycling. In this work, we observe substantial capacity fade for $Li_2MnP_2S_6$ from the second to 15th cycles. Recent work with $Li_2Fe_{0.8}Mn_{0.2}P_2S_6$ showed a massive first cycle capacity of 1.65 Li before

https://doi.org/10.1021/acs.chemmater.4c02366
Chem. Mater. 2024, 36, 9947−9958

achieving a relatively stable capacity of ∼1 Li in subsequent cycles. While the electronic structure analysis presented in this work is helpful to understand which states are likely to be involved in redox, additional experimental and computational work should strive to understand and control the electrochemically induced phase transformations occurring in these materials.

CONCLUSIONS

In this work, an I_2-based metathesis reaction was used to synthesize $Li_2MP_2S_6$ (M = Mn, Fe, and Co) phases, of which $Li_2MnP_2S_6$ is a newly reported compound. Electrochemical measurements demonstrate Li extraction from $Li_2FeP_2S_6$ and $Li_2MnP_2S_6$ at ∼3 V with capacities of 40 and 70 mAh/g, respectively. Experimental characterization and extensive electronic structure calculations were used to characterize and understand the redox mechanism in $Li_2FeP_2S_6$ and $Li_2MnP_2S_6$ cathode materials. For M = Fe, it is mainly the Fe states that account for charge compensation of the first Li^+ extracted from $Li_2FeP_2S_6$. In contrast, for M = Mn, antibonding Mn−S and S−S states are oxidized and accompanied by significant rehybridization of Mn and S states during charging. Although Mn K-edge XANES and Bader charge analysis show that Mn valence is unchanged during charging, the computed electronic structures, charge densities, and magnetic moments show that both Mn and S states participate in redox. This work reinforces the promise of high-voltage sulfide-based cathodes for Li-ion batteries with the potential for significant capacity by combining both cationic and anionic redox.

METHODS

Experimental Section. $Li_2MP_2S_6$ (M = Mn, Fe, and Co) synthesis was attempted by heating the starting materials in an evacuated quart tube. Li_2S (Mitsuwa Chemical, 99.9%), $MnCl_2$ (Strem Chemicals, 99.995%), $FeCl_2$ (Strem Chemicals, 98%), MnI_2 (Kojundo Chemical, 99.9%), FeI_2 (Thermo Fisher Scientific, 97%), CoI_2 (Strem Chemicals, 95%), NiI_2 (Kojundo Chemical, 99.9%) and P_2S_5 (Sigma-Aldrich, 99%) were used as the starting materials. Li_2S (0.79−1.2 g), MX_2 (3.2−5.4 g of MI_2) (M = Mn, Fe, Co and X = Cl, I) and P_2S_5 (3.8−5.6 g) were mixed with stoichiometric amount by an agate mortar. The total amount was 10 g each. The mixtures were sealed in evacuated quart tubes of a 10 mm diameter and 200 mm length, and the tubes were heated at 460 °C for 12 h in a tubular furnace. To prevent the buildup of high pressure caused by I_2 byproduct inside the tubes, the end of the tubes was positioned outside the tubular furnace during the heating process. The flux was then removed by THF and methanol. X-ray diffraction (XRD) patterns of the samples were recorded using an X-ray diffractometer with CuKα radiation source (MiniFlex600, Rigaku) or synchrotron X-ray sources at the SPring-8 BL02B2 (2022A1296) or BL13XU (2024A2366).[59] The crystal structure of $Li_2MnP_2S_6$ was determined by Rietveld analysis using RIETAN.[60] Neutron diffraction of $Li_2MnP_2S_6$ sealed in a vanadium metal vessel was performed at a wavelength of 1.34177 Å using the angle-dispersive-type diffractometer, HERMES at JRR3 at the Japan Atomic Energy Agency.[61] The crystal structure of $Li_2MnP_2S_6$ was analyzed by TOPAS.[62] The morphologies and compositions (M, P and S) of the obtained samples were investigated by using scanning electron microscopy with energy-dispersive X-ray spectroscopy (SEM/EDX; JSM-6510 LA, JEOL). The compositions of Li and M were examined by inductively coupled plasma (ICP) techniques.

The all-solid-state batteries containing the obtained powders as the cathode materials were constructed according to previous reports[8] to investigate the electrochemical behavior of the samples. Li_3PS_4 glass powders and In sheets were used as the solid electrolyte and the anode materials, respectively. A solid electrolyte was used to alleviate the possibility of S dissolution in a liquid electrolyte at high voltage. The composite cathodes were prepared by mixing the obtained powders, Li_3PS_4 glass powders, and vapor-grown carbon fibers (VGCF, Showa Denko) with the weight ratio of 50:40:10 in an agate mortar. The composites were used as the cathode layer (10 mg). The charge−discharge behavior was measured by using a charge−discharge measuring device (Scribner Associates, 580 battery-type system) under a current density of 6.4 μA cm^{-2} at 60 °C. In addition, Galvanostatic intermittent titration technique (GITT) was applied to investigate the voltage of the batteries in detail without the effect of overpotential. The quasi-equilibrium potential of $Li_xMP_2S_6$ during the entire charging and discharging process was obtained under a current density of 12.7 μA/cm^2 at 60 °C by constructing the Li−In | Li_3PS_4 | $Li_2MP_2S_6$ all-solid-state cell (Figure S8). The lithium extraction/insertion experiment was conducted for a duration of 20 min, followed by a waiting period of another 20 min. The cutoff voltage was set to 4.0 V vs Li−In for charging and 0.5 V vs Li−In for discharging. To clarify the reaction mechanism of $Li_2MP_2S_6$, the XRD patterns of the composite cathodes containing $Li_2MP_2S_6$ were measured before and after charge/discharge at SPring-8 BL13XU beamline (2023A1042). X-ray absorption near-edge structure (XANES) of Mn K-edge was measured at the SPring-8 BL14B2 (proposal No. 2022B1585). S K-edge XANES were measured at the SPring-8 BL27SU.

Computational Details. All DFT calculations were performed using the Vienna Ab Initio Simulation Package (VASP 6.4.1)[63,64] and the projector augmented wave (PAW) method.[65,66] A plane-wave energy cutoff of 520 eV, and a Γ-centered k-point grid with a minimum spacing between k-points of 0.3 Å^{-1} (KSPACING in VASP), were used for all calculations. To explore various orderings for a specific Li concentration in a given composition, the r^{2}SCAN meta-generalized gradient approximation (meta-GGA) density functional[36] was applied. Meta-GGA functionals have been shown to achieve high accuracy for voltage, energy, and electronic density of states predictions for battery materials,[67,68] and they address many of the typical shortcomings of GGA functionals.[69,70] To correct lingering self-interaction errors for the voltage calculation, the ground state configurations predicted by r^{2}SCAN were then recalculated by the r^{2}SCAN+U[70,71] density functional with U values of 2.9 and 2.1 eV for Fe and Mn, respectively.[69] We then employed the HSE06 hybrid functional to accurately capture the electronic structures of the r^{2}SCAN-relaxed structures.[40] All calculations were initialized in high-spin ferromagnetic and 6 high-spin antiferromagnetic initial configurations. The convergence criteria were set as 3×10^{-6} eV for electronic optimization and 0.03 eV·Å^{-1} for ionic relaxation.

To determine the equilibrium structures for thermodynamic and electronic structure analysis, we performed a detailed investigation of Li/Mn orderings in $Li_2MnP_2S_6$. Starting from the experimental structure in a trigonal unit cell (space group P$\bar{3}$1m), we generated a $2 \times 1 \times 2$ supercell. There are two Wyckoff sites for Li in this structure — 2c and 2d — with 8 of each of these sites per supercell. All possible Li occupations on positions 2c and 2d were enumerated by first defining the Li occupation ratio $p = n_{2c}/n_{2d}$, where n_{2c} and n_{2d} are the occupation numbers of Li on 2c and 2d positions, respectively. As p approaches 0, Li is depleted from position 2c first. When p increases, Li is extracted first from 2d. Next, we listed the combinations (n_{2c}, n_{2d}) that satisfy a given Li concentration, x, in $Li_xMnP_2S_6$ (where x = 0, $\frac{1}{4}$, $\frac{1}{2}$, $\frac{3}{4}$, ..., 2) under the constraints that $0 \le n_{2c} \le \min\left(1, \frac{x}{2}\right)$, $0 \le n_{2d} \le \min\left(\frac{1}{2}, \frac{x}{2}\right)$, and $n_{2c} + n_{2d} = \frac{x}{2}$. To determine the specific ordered phases to compute with DFT, we enumerated through the symmetrically distinct orderings and computed the four orderings with the lowest electrostatic energy, evaluated using the Ewald method as implemented in pymatgen.[72] These results suggest that the 2c site is depleted first (Figure S6). For $Li_2FeP_2S_6$ and $Li_2Fe_{0.75}Mn_{0.25}P_2S_6$, we used the $Li_2MnP_2S_6$ ground-state orderings. To evaluate the energies of partially lithiated phases ($Li_xFeP_2S_6$ and $Li_xFe_{0.75}Mn_{0.25}P_2S_6$), we used the lowest energy $Li_xMnP_2S_6$ structures

https://doi.org/10.1021/acs.chemmater.4c02366
Chem. Mater. 2024, 36, 9947−9958

that are topotactically related to the as-synthesized, fully discharged phase.

For the thermodynamic stability analysis, all competing phases in each Li−*M*−P−S phase diagram were collected from the Materials Project database[73] and recomputed using the aforementioned calculation settings (r^{2}SCAN). For the reaction energies, formation enthalpies were obtained from experimental data[38] where available (all phases except $Li_2MP_2S_6$), otherwise DFT calculations were used ($Li_2MP_2S_6$). These formation enthalpies were transformed to finite temperature free energies using a previously published model accounting for vibrational entropy effects.[74]

The LOBSTER[75] package was used for DOS and COHP analysis and the Bader[76] method was used for charge analysis. Pymatgen was used for preparing and analyzing calculations.[72] Structures and charge densities were analyzed using VESTA.[77]

■ ASSOCIATED CONTENT

Supporting Information

The Supporting Information is available free of charge at https://pubs.acs.org/doi/10.1021/acs.chemmater.4c02366.

XRD patterns of $Li_2MP_2S_6$ from chloride-assisted and traditional solid-state synthesis, photo of the quartz tube, calculated thermodynamic driving forces of $Li_2MP_2S_6$ (M = Fe, Mn, and Co) from various synthesis routes, SEM images of as-synthesized $Li_2MP_2S_6$ (*M* = Fe, Mn, and Co), details of elemental analysis from EDX and ICP measurements, coordinates of Wyckoff position, displacement factors, occupancy, variation of lattice parameters, and bonding lengths of $Li_2MnP_2S_6$ from XRD analysis, site energy penalty for Li/*M* ordering in $Li_2MP_2S_6$ (*M* = Fe and Mn), GITT traces of $Li_2MnP_2S_6$ during charging and discharging process, the schematic of cell configuration, quasi-equilibrium voltage of $Li_2MP_2S_6$ (*M* = Co and Ni), calculated convex hull of mixing energies $Li_2MP_2S_6$ (*M* = Fe and Mn), DOS and COHP of $LiFeP_2S_6$, $LiMnP_2S_6$, fully discharged $Li_2Fe_{1-y}Mn_yP_2S_6$, and evaluation of $Li_2Fe_{0.75}Mn_{0.25}P_2S_6$, variation in calculated Bader charge and optimized average magnetic moment of $Li_xMnP_2S_6$ (PDF)

■ AUTHOR INFORMATION

Corresponding Authors

Akira Miura − *Faculty of Engineering, Hokkaido University, Sapporo 060-8628, Japan;* orcid.org/0000-0003-0388-9696; Email: amiura@eng.hokudai.ac.jp

Christopher J. Bartel − *Department of Chemical Engineering and Materials Science, University of Minnesota, Minneapolis, Minnesota 55455, United States;* orcid.org/0000-0002-5198-5036; Email: cbartel@umn.edu

Authors

Yi-Ting Cheng − *Department of Chemical Engineering and Materials Science, University of Minnesota, Minneapolis, Minnesota 55455, United States;* orcid.org/0000-0002-1670-9933

Yuta Fujii − *Faculty of Engineering, Hokkaido University, Sapporo 060-8628, Japan;* orcid.org/0000-0002-8381-4119

Yu Nomata − *Graduate School of Chemical Sciences and Engineering, Hokkaido University, Sapporo 060-8628, Japan*

Madhulika Mazumder − *Department of Chemical Engineering and Materials Science, University of Minnesota, Minneapolis, Minnesota 55455, United States*

Nataly Carolina Rosero-Navarro − *Faculty of Engineering, Hokkaido University, Sapporo 060-8628, Japan; Instituto de Cerámica y Vidrio, CSIC, Madrid 28049, Spain;* orcid.org/0000-0001-6838-2875

Aichi Yamashita − *Department of Physics, Tokyo Metropolitan University, Tokyo 192-0397, Japan*

Yoshikazu Mizuguchi − *Department of Physics, Tokyo Metropolitan University, Tokyo 192-0397, Japan;* orcid.org/0000-0002-4771-7805

Chikako Moriyoshi − *Graduate School of Advanced Science and Engineering, Hiroshima University, Hiroshima 739-8526, Japan;* orcid.org/0000-0002-4508-5779

Takato Mitsudome − *Department of Materials Engineering Science, Graduate School of Engineering Science, Osaka University, Osaka 560-8531, Japan;* orcid.org/0000-0003-3071-8243

Toshiaki Ina − *Spectroscopy Division, Japan Synchrotron Radiation Research Institute, Sayo, Hyogo 679-5198, Japan*

Kiyofumi Nitta − *Spectroscopy Division, Japan Synchrotron Radiation Research Institute, Sayo, Hyogo 679-5198, Japan*

Kiyoharu Tadanaga − *Faculty of Engineering, Hokkaido University, Sapporo 060-8628, Japan;* orcid.org/0000-0002-3319-4353

Complete contact information is available at: https://pubs.acs.org/10.1021/acs.chemmater.4c02366

Author Contributions

◆Y.-T.C., Y.F., and Y.N. contributed equally.

Notes

The authors declare no competing financial interest.

■ ACKNOWLEDGMENTS

Y.-T.C, M.M, and C.J.B. gratefully acknowledge support from the University of Minnesota in the form of new faculty start-up. The authors acknowledge the Minnesota Supercomputing Institute (MSI) at the University of Minnesota for providing resources that contributed to the research results reported within this paper. This work used Bridges-2 at Pittsburgh Supercomputing Center through allocation MAT230036 from the Advanced Cyberinfrastructure Coordination Ecosystem: Services & Support (ACCESS) program, which is supported by National Science Foundation grants #2138259, #2138286, #2138307, #2137603, and #2138296. This research was partially supported by KAKENHI Grant Number JP20KK0124(AM) and JST PRESTO (Grant Numbers JPMJPR21Q8(AM) and JPMJPR21Q9(TM)).

■ REFERENCES

(1) Ozawa, K. Lithium-Ion Rechargeable Batteries with LiCoO2 and Carbon Electrodes: The LiCoO2/C System. *Solid State Ion.* **1994**, *69* (3−4), 212−221.

(2) Mizushima, K.; Jones, P.; Wiseman, P.; Goodenough, J. B. LixCoO2 (0< X<-1): A New Cathode Material for Batteries of High Energy Density. *Mater. Res. Bull.* **1980**, *15* (6), 783−789.

(3) Seo, D.-H.; Lee, J.; Urban, A.; Malik, R.; Kang, S.; Ceder, G. The Structural and Chemical Origin of the Oxygen Redox Activity in Layered and Cation-Disordered Li-Excess Cathode Materials. *Nat. Chem.* **2016**, *8* (7), 692−697.

(4) Ohzuku, T.; Nagayama, M.; Tsuji, K.; Ariyoshi, K. High-Capacity Lithium Insertion Materials of Lithium Nickel Manganese Oxides for Advanced Lithium-Ion Batteries: Toward Rechargeable Capacity More than 300 mA Hg− 1. *J. Mater. Chem.* **2011**, *21* (27), 10179−10188.

(5) Thackeray, M. M.; Kang, S.-H.; Johnson, C. S.; Vaughey, J. T.; Benedek, R.; Hackney, S. Li 2 MnO 3-Stabilized LiMO 2 (M= Mn, Ni, Co) Electrodes for Lithium-Ion Batteries. *J. Mater. Chem.* **2007**, *17* (30), 3112−3125.
(6) Manthiram, A. A Reflection on Lithium-Ion Battery Cathode Chemistry. *Nat. Commun.* **2020**, *11* (1), 1550.
(7) Grayfer, E. D.; Pazhetnov, E. M.; Kozlova, M. N.; Artemkina, S. B.; Fedorov, V. E. Anionic Redox Chemistry in Polysulfide Electrode Materials for Rechargeable Batteries. *ChemSusChem* **2017**, *10* (24), 4805−4811.
(8) Zarabadi-Poor, P.; Lim, J.; Wang, X.; Bocarsly, J. D.; Daniels, L. M.; Pateli, I. M.; Chen, R.; Claridge, J. B.; Grey, C. P.; Morgan, B. J.; Hardwick, L. J.; Rosseinsky, M. J.; Islam, M. S. Accessing Polyanionic Redox in High Voltage Li-Rich Thiophosphates. *ChemRxiv* **2023-02−21.**.
(9) Saha, S.; Assat, G.; Sougrati, M. T.; Foix, D.; Li, H.; Vergnet, J.; Turi, S.; Ha, Y.; Yang, W.; Cabana, J.; Rousse, G.; Abakumov, A. M.; Tarascon, J. M. Exploring the Bottlenecks of Anionic Redox in Li-Rich Layered Sulfides. *Nat. Energy* **2019**, *4* (11), 977−987.
(10) Zak, J. J.; Kim, S. S.; Laskowski, F. A. L.; See, K. A. An Exploration of Sulfur Redox in Lithium Battery Cathodes. *J. Am. Chem. Soc.* **2022**, *144* (23), 10119−10132.
(11) Marchandier, T.; Mariyappan, S.; Kirsanova, M. A.; Abakumov, A. M.; Rousse, G.; Foix, D.; Sougrati, M. T.; Doublet, M. L.; Tarascon, J. M. Triggering Anionic Redox Activity in Li3NbS4 Through Cationic Disordering or Substitution. *Adv. Energy Mater.* **2022**, *12* (41), 2201417.
(12) Leube, B. T.; Robert, C.; Foix, D.; Porcheron, B.; Dedryvère, R.; Rousse, G.; Salager, E.; Cabelguen, P. E.; Abakumov, A. M.; Vezin, H.; Doublet, M. L.; Tarascon, J. M. Activation of Anionic Redox in D0 Transition Metal Chalcogenides by Anion Doping. *Nat. Commun.* **2021**, *12* (1), 5485.
(13) Pan, M.; Hakari, T.; Sakuda, A.; Hayashi, A.; Suginaka, Y.; Mori, S.; Tatsumisago, M. Electrochemical Properties of All-Solid-State Lithium Batteries with Amorphous FeSx-Based Composite Positive Electrodes Prepared via Mechanochemistry. *Electrochemistry* **2018**, *86* (4), 175−178.
(14) Ulissi, U.; Ito, S.; Hosseini, S. M.; Varzi, A.; Aihara, Y.; Passerini, S. High Capacity All-Solid-State Lithium Batteries Enabled by Pyrite-Sulfur Composites. *Adv. Energy Mater.* **2018**, *8* (26), 1801462.
(15) Zhang, Q.; Yao, X.; Mwizerwa, J. P.; Huang, N.; Wan, H.; Huang, Z.; Xu, X. FeS Nanosheets as Positive Electrodes for All-Solid-State Lithium Batteries. *Solid State Ion.* **2018**, *318*, 60−64.
(16) Fujii, Y.; Miura, A.; Rosero-Navarro, N. C.; Higuchi, M.; Tadanaga, K. FePS3 Electrodes in All-Solid-State Lithium Secondary Batteries Using Sulfide-Based Solid Electrolytes. *Electrochim. Acta* **2017**, *241*, 370−374.
(17) Hansen, C. J.; Zak, J. J.; Martinolich, A. J.; Ko, J. S.; Bashian, N. H.; Kaboudvand, F.; Van der Ven, A.; Melot, B. C.; Nelson Weker, J.; See, K. A. Multielectron, Cation and Anion Redox in Lithium-Rich Iron Sulfide Cathodes. *J. Am. Chem. Soc.* **2020**, *142* (14), 6737−6749.
(18) Fujii, Y.; Kobayashi, M.; Miura, A.; Rosero-Navarro, N. C.; Li, M.; Sun, J.; Kotobuki, M.; Lu, L.; Tadanaga, K. Fe−P−S Electrodes for All-Solid-State Lithium Secondary Batteries Using Sulfide-Based Solid Electrolytes. *J. Power Sources* **2020**, *449*, No. 227576.
(19) Takada, K.; Michiue, Y.; Inada, T.; Kajiyama, A.; Kouguchi, M.; Kondo, S.; Watanabe, M.; Tabuchi, M. Lithium Iron Thio-Phosphate: A New 3 V Sulfide Cathode. *Solid State Ion.* **2003**, *159* (3), 257−263.
(20) Gutierrez, A.; Benedek, N. A.; Manthiram, A. Crystal-Chemical Guide for Understanding Redox Energy Variations of M2+/3+ Couples in Polyanion Cathodes for Lithium-Ion Batteries. *Chem. Mater.* **2013**, *25* (20), 4010−4016.
(21) Zhang, L.; Sun, D.; Kang, J.; Wang, H.-T.; Hsieh, S.-H.; Pong, W.-F.; Bechtel, H. A.; Feng, J.; Wang, L.-W.; Cairns, E. J.; Guo, J. Tracking the Chemical and Structural Evolution of the TiS2 Electrode in the Lithium-Ion Cell Using Operando X-Ray Absorption Spectroscopy. *Nano Lett.* **2018**, *18* (7), 4506−4515.
(22) Sakuda, A.; Ohara, K.; Fukuda, K.; Nakanishi, K.; Kawaguchi, T.; Arai, H.; Uchimoto, Y.; Ohta, T.; Matsubara, E.; Ogumi, Z.; Okumura, T.; Kobayashi, H.; Kageyama, H.; Shikano, M.; Sakaebe, H.; Takeuchi, T. Amorphous Metal Polysulfides: Electrode Materials with Unique Insertion/Extraction Reactions. *J. Am. Chem. Soc.* **2017**, *139* (26), 8796−8799.
(23) Zhong, L.; Chen, H.; Xie, W.; Jia, W.; Xiao, Y.; Cheng, B.; Lin, L.; Lei, S. Intercalation and Defect Engineering of Layered MnPS3 for Greatly Enhanced Capacity and Stability in Sodium-Ion Batteries. *Chem. Eng. J.* **2024**, *481*, No. 148370.
(24) Shen, H.; Cai, Y.; Ma, Z.; Wang, P.; Guo, B.; Cheng, J.; Li, Q.; Wang, H.; Liu, Z.; Nie, A.; Wu, J. Layered Manganese Phosphorus Trisulfides for High-performance Lithium-ion Batteries and the Storage Mechanism. *Carbon Energy* **2023**, *5* (3), No. e290.
(25) Cheng, M.; Lee, Y.-S.; Iyer, A. K.; Chica, D. G.; Qian, E. K.; Shehzad, M. A.; dos Reis, R.; Kanatzidis, M. G.; Dravid, V. P. Mixed Metal Thiophosphate Fe2−xCoxP2S6: Role of Structural Evolution and Anisotropy. *Inorg. Chem.* **2021**, *60* (22), 17268−17275.
(26) Zhu, M.; Kou, H.; Wang, K.; Wu, H.; Ding, D.; Zhou, G.; Ding, S. Promising Functional Two-Dimensional Lamellar Metal Thiophosphates: Synthesis Strategies. *Properties and Applications. Mater. Horiz.* **2020**, *7* (12), 3131−3160.
(27) Fujii, Y.; Miura, A.; Rosero-Navarro, N. C.; Mizuguchi, Y.; Moriyoshi, C.; Kuroiwa, Y.; Higuchi, M.; Tadanaga, K. Reaction Mechanism of FePS3 Electrodes in All-Solid-State Lithium Secondary Batteries Using Sulfide-Based Solid Electrolytes. *J. Electrochem. Soc.* **2018**, *165* (13), A2948.
(28) Kuzminskii, Y. V.; Voronin, B.; Redin, N. Iron and Nickel Phosphorus Trisulfides as Electroactive Materials for Primary Lithium Batteries. *J. Power Sources* **1995**, *55* (2), 133−141.
(29) Foot, P.; Suradi, J.; Lee, P. Optical and Electronic Properties of the Layered Semiconductors NiPS3 and FePS3. *Mater. Res. Bull.* **1980**, *15* (2), 189−193.
(30) Hood, Z. D.; Kates, C.; Kirkham, M.; Adhikari, S.; Liang, C.; Holzwarth, N. A. Structural and Electrolyte Properties of Li4P2S6. *Solid State Ion.* **2016**, *284*, 61−70.
(31) Mercier, R.; Malugani, J. P.; Fahys, B.; Douglande, J.; Robert, G. Synthese, Structure Cristalline et Analyse Vibrationnelle de l'hexathiohypodiphosphate de Lithium Li4P2S6. *J. Solid State Chem.* **1982**, *43* (2), 151−162.
(32) Diethrich, T. J.; Zavalij, P. Y.; Gnewuch, S.; Rodriguez, E. E. Orbital Contribution to Paramagnetism and Noninnocent Thiophosphate Anions in Layered Li2MP2S6 Where M= Fe and Co. *Inorg. Chem.* **2021**, *60* (14), 10280−10290.
(33) Neilson, J. R.; McDermott, M. J.; Persson, K. A. Modernist Materials Synthesis: Finding Thermodynamic Shortcuts with Hyperdimensional Chemistry. *J. Mater. Res.* **2023**, *38*, 2885−2893.
(34) Miura, A.; Ito, H.; Bartel, C. J.; Sun, W.; Rosero-Navarro, N. C.; Tadanaga, K.; Nakata, H.; Maeda, K.; Ceder, G. Selective Metathesis Synthesis of MgCr 2 S 4 by Control of Thermodynamic Driving Forces. *Mater. Horiz.* **2020**, *7* (5), 1310−1316.
(35) Sundaramoorthy, S.; Gerasimchuk, N.; Ghosh, K.; Kelley, S. P.; Choudhury, A. Li2MP2S6: Building-Block Approach to a Family of 2D Non-van Der Waals-Layered Materials and Their Water, Ammonia, and Ion Intercalation Properties. *Chem. Mater.* **2024**, *36* (8), 3574−3587.
(36) Furness, J. W.; Kaplan, A. D.; Ning, J.; Perdew, J. P.; Sun, J. Accurate and Numerically Efficient r2SCAN Meta-Generalized Gradient Approximation. *J. Phys. Chem. Lett.* **2020**, *11* (19), 8208−8215.
(37) Bartel, C. J. Review of Computational Approaches to Predict the Thermodynamic Stability of Inorganic Solids. *J. Mater. Sci.* **2022**, *57* (23), 10475−10498.
(38) Barin, I. *Thermochemical Data of Pure Substances*; VCH: 1989; Vol. *304*.
(39) Hakari, T.; Nagao, M.; Hayashi, A.; Tatsumisago, M. All-Solid-State Lithium Batteries with Li3PS4 Glass as Active Material. *J. Power Sources* **2015**, *293*, 721−725.

https://doi.org/10.1021/acs.chemmater.4c02366
Chem. Mater. 2024, 36, 9947−9958

(40) Krukau, A. V.; Vydrov, O. A.; Izmaylov, A. F.; Scuseria, G. E. Influence of the Exchange Screening Parameter on the Performance of Screened Hybrid Functionals. *J. Chem. Phys.* **2006**, *125* (22), 224106.
(41) Steinberg, S.; Dronskowski, R. The Crystal Orbital Hamilton Population (COHP) Method as a Tool to Visualize and Analyze Chemical Bonding in Intermetallic Compounds. *Crystals* **2018**, *8* (5), 225.
(42) Deringer, V. L.; Tchougréeff, A. L.; Dronskowski, R. Crystal Orbital Hamilton Population (COHP) Analysis As Projected from Plane-Wave Basis Sets. *J. Phys. Chem. A* **2011**, *115* (21), 5461−5466.
(43) Dronskowski, R.; Bloechl, P. E. Crystal Orbital Hamilton Populations (COHP): Energy-Resolved Visualization of Chemical Bonding in Solids Based on Density-Functional Calculations. *J. Phys. Chem.* **1993**, *97* (33), 8617−8624.
(44) Hoang, K.; Johannes, M. Defect Physics in Complex Energy Materials. *J. Phys.: Condens. Matter* **2018**, *30* (29), 293001.
(45) Hu, E.; Li, Q.; Wang, X.; Meng, F.; Liu, J.; Zhang, J. N.; Page, K.; Xu, W.; Gu, L.; Xiao, R.; Li, H.; Huang, X.; Chen, L.; Yang, W.; Yu, X.; Yang, X. Q. Oxygen-Redox Reactions in LiCoO2 Cathode without O−O Bonding during Charge-Discharge. *Joule* **2021**, *5* (3), 720−736.
(46) Manos, M. J.; Kanatzidis, M. G. Highly Efficient and Rapid Cs+ Uptake by the Layered Metal Sulfide K2xMnxSn3−xS6 (KMS-1). *J. Am. Chem. Soc.* **2009**, *131* (18), 6599−6607.
(47) Wolverton, C.; Zunger, A. First-Principles Prediction of Vacancy Order-Disorder and Intercalation Battery Voltages in Li x CoO 2. *Phys. Rev. Lett.* **1998**, *81* (3), 606.
(48) Odahara, J.; Sun, W.; Miura, A.; Rosero-Navarro, N. C.; Nagao, M.; Tanaka, I.; Ceder, G.; Tadanaga, K. Self-Combustion Synthesis of Novel Metastable Ternary Molybdenum Nitrides. *ACS Mater. Lett.* **2019**, *1* (1), 64−70.
(49) Martinolich, A. J.; Neilson, J. R. Toward Reaction-by-Design: Achieving Kinetic Control of Solid State Chemistry with Metathesis. *Chem. Mater.* **2017**, *29* (2), 479−489.
(50) Todd, P. K.; McDermott, M. J.; Rom, C. L.; Corrao, A. A.; Denney, J. J.; Dwaraknath, S. S.; Khalifah, P. G.; Persson, K. A.; Neilson, J. R. Selectivity in Yttrium Manganese Oxide Synthesis via Local Chemical Potentials in Hyperdimensional Phase Space. *J. Am. Chem. Soc.* **2021**, *143* (37), 15185−15194.
(51) Liu, X.; Krott, M.; Müller, P.; Hu, C.; Lueken, H.; Dronskowski, R. Synthesis, Crystal Structure, and Properties of MnNCN, the First Carbodiimide of a Magnetic Transition Metal. *Inorg. Chem.* **2005**, *44* (9), 3001−3003.
(52) Szymanski, N. J.; Bartel, C. J. Computationally Guided Synthesis of Battery Materials. *ACS Energy Lett.* **2024**, *9*, 2902−2911.
(53) Kim, S. S.; Agyeman-Budu, D. N.; Zak, J. J.; Dawson, A.; Yan, Q.; Cában-Acevedo, M.; Wiaderek, K. M.; Yakovenko, A. A.; Yao, Y.; Irshad, A.; Narayan, S. R.; Luo, J.; Nelson Weker, J.; Tolbert, S. H.; See, K. A. Promoting Reversibility of Multielectron Redox in Alkali-Rich Sulfide Cathodes through Cryomilling. *Chem. Mater.* **2022**, *34* (7), 3236−3245.
(54) Sun, X.; Bonnick, P.; Duffort, V.; Liu, M.; Rong, Z.; Persson, K. A.; Ceder, G.; Nazar, L. F. A High Capacity Thiospinel Cathode for Mg Batteries. *Energy Environ. Sci.* **2016**, *9* (7), 2273−2277.
(55) Padhi, A.; Manivannan, V.; Goodenough, J. Tuning the Position of the Redox Couples in Materials with NASICON Structure by Anionic Substitution. *J. Electrochem. Soc.* **1998**, *145* (5), 1518.
(56) Muraliganth, T.; Manthiram, A. Understanding the Shifts in the Redox Potentials of Olivine LiM1− y M y PO4 (M= Fe, Mn, Co, and Mg) Solid Solution Cathodes. *J. Phys. Chem. C* **2010**, *114* (36), 15530−15540.
(57) Arroyo-de Dompablo, M.; Armand, M.; Tarascon, J.; Amador, U. On-Demand Design of Polyoxianionic Cathode Materials Based on Electronegativity Correlations: An Exploration of the Li2MSiO4 System (M= Fe, Mn, Co, Ni). *Electrochem. Commun.* **2006**, *8* (8), 1292−1298.
(58) Blanc, L.; Bartel, C. J.; Kim, H.; Tian, Y.; Kim, H.; Miura, A.; Ceder, G.; Nazar, L. F. Toward the Development of a High-Voltage Mg Cathode Using a Chromium Sulfide Host. *ACS Mater. Lett.* **2021**, *3* (8), 1213−1220.
(59) Kawaguchi, S.; Kobayashi, S.; Yamada, H.; Ashitani, H.; Takemoto, M.; Imai, Y.; Hatsui, T.; Sugimoto, K.; Sakata, O. High-throughput and High-resolution Powder X-ray Diffractometer Consisting of Six Sets of 2D CdTe Detectors with Variable Sample-to-detector Distance and Innovative Automation System. *J. Synchrotron Radiat.* **2024**, *31* (4), 955−967.
(60) Izumi, F.; Momma, K. Three-Dimensional Visualization in Powder Diffraction. *Solid State Phenom.* **2007**, *130*, 15−20.
(61) Nambu, Y.; Ikeda, Y.; Taniguchi, T.; Ohkawara, M.; Avdeev, M.; Fujita, M. Neutron Powder Diffractometer HERMES—After the Decade-Long Shutdown. *J. Phys. Soc. Jpn.* **2024**, *93* (9), No. 091005.
(62) Coelho, A. A. TOPAS and TOPAS-Academic: An Optimization Program Integrating Computer Algebra and Crystallographic Objects Written in C++. *J. Appl. Crystallogr.* **2018**, *51* (1), 210−218.
(63) Kresse, G.; Furthmüller, J. Efficiency of Ab-Initio Total Energy Calculations for Metals and Semiconductors Using a Plane-Wave Basis Set. *Comput. Mater. Sci.* **1996**, *6* (1), 15−50.
(64) Kresse, G.; Furthmüller, J. Efficient Iterative Schemes for Ab Initio Total-Energy Calculations Using a Plane-Wave Basis Set. *Phys. Rev. B* **1996**, *54* (16), 11169.
(65) Kresse, G.; Joubert, D. From Ultrasoft Pseudopotentials to the Projector Augmented-Wave Method. *Phys. Rev. B* **1999**, *59* (3), 1758−1775.
(66) Blöchl, P. E. Projector Augmented-Wave Method. *Phys. Rev. B* **1994**, *50* (24), 17953−17979.
(67) Chakraborty, A.; Dixit, M.; Aurbach, D.; Major, D. T. Predicting Accurate Cathode Properties of Layered Oxide Materials Using the SCAN Meta-GGA Density Functional. *npj Comput. Mater.* **2018**, *4* (1), 60.
(68) He, Q.; Yu, B.; Li, Z.; Zhao, Y. Density Functional Theory for Battery Materials. *Energy Environ. Mater.* **2019**, *2* (4), 264−279.
(69) Swathilakshmi, S.; Devi, R.; Sai Gautam, G. Performance of the r2SCAN Functional in Transition Metal Oxides. *J. Chem. Theory Comput.* **2023**, *19* (13), 4202−4215.
(70) Sai Gautam, G.; Carter, E. A. Evaluating Transition Metal Oxides within DFT-SCAN and SCAN+ U Frameworks for Solar Thermochemical Applications. *Phys. Rev. Mater.* **2018**, *2* (9), No. 095401.
(71) Long, O. Y.; Sai Gautam, G.; Carter, E. A. Evaluating Optimal U for 3 d Transition-Metal Oxides within the SCAN+ U Framework. *Phys. Rev. Mater.* **2020**, *4* (4), No. 045401.
(72) Ong, S. P.; Richards, W. D.; Jain, A.; Hautier, G.; Kocher, M.; Cholia, S.; Gunter, D.; Chevrier, V. L.; Persson, K. A.; Ceder, G. Python Materials Genomics (Pymatgen): A Robust, Open-Source Python Library for Materials Analysis. *Comput. Mater. Sci.* **2013**, *68*, 314−319.
(73) Jain, A.; Ong, S. P.; Hautier, G.; Chen, W.; Richards, W. D.; Dacek, S.; Cholia, S.; Gunter, D.; Skinner, D.; Ceder, G.; Persson, K. A. Commentary: The Materials Project: A Materials Genome Approach to Accelerating Materials Innovation. *APL Mater.* **2013**, *1* (1), No. 011002.
(74) Bartel, C. J.; Millican, S. L.; Deml, A. M.; Rumptz, J. R.; Tumas, W.; Weimer, A. W.; Lany, S.; Stevanović, V.; Musgrave, C. B.; Holder, A. M. Physical Descriptor for the Gibbs Energy of Inorganic Crystalline Solids and Temperature-Dependent Materials Chemistry. *Nat. Commun.* **2018**, *9* (1), 4168.
(75) Maintz, S.; Deringer, V. L.; Tchougréeff, A. L.; Dronskowski, R. LOBSTER: A Tool to Extract Chemical Bonding from Plane-wave Based DFT. *J. Comput. Chem.* **2016**, *37* (11), 1030−1035.
(76) Henkelman, G.; Arnaldsson, A.; Jónsson, H. A Fast and Robust Algorithm for Bader Decomposition of Charge Density. *Comput. Mater. Sci.* **2006**, *36* (3), 354−360.
(77) Momma, K.; Izumi, F. VESTA 3 for Three-Dimensional Visualization of Crystal, Volumetric and Morphology Data. *J. Appl. Crystallogr.* **2011**, *44* (6), 1272−1276.

https://doi.org/10.1021/acs.chemmater.4c02366
Chem. Mater. 2024, 36, 9947−9958